



# Macro-micro analysis of mechanical properties of $\text{Al}_{0.6}\text{CoCrFeNi}$ high-entropy alloy particle-reinforced Al-based composites

Zhanwei Yuan<sup>a,\*</sup>, Zhe Ma<sup>a</sup>, Hao Zhang<sup>b</sup>, Kai Wang<sup>a</sup>, Yuan Yu<sup>c,\*\*</sup>, Shurong Li<sup>a</sup>, Xuemin Zhang<sup>a</sup>, Jingyi Wang<sup>a</sup>, Danli Zhang<sup>d</sup>

<sup>a</sup> School of Materials Science and Engineering, Chang'an University, Xi'an, Shaanxi, 710064, China

<sup>b</sup> CNPC Tubular Goods Research Institute, Xi'an, Shaanxi, 710064, China

<sup>c</sup> State Key Laboratory of Solid Lubrication, Lanzhou Institute of Chemical Physics, Chinese Academy of Sciences, Lanzhou, 730000, PR China

<sup>d</sup> Center for Advancing Materials Performance from the Nanoscale (CAMP-Nano), State Key Laboratory for Mechanical Behavior of Materials, Xi'an Jiaotong University, Xi'an, 710049, China



## ARTICLE INFO

### Keywords:

Aluminum matrix composites  
NanoBlitz 3D method  
Mechanical property mapping images  
Mathematical models

## ABSTRACT

In this study,  $\text{Al}_{0.6}\text{CoCrFeNi}$  high-entropy alloy particle-reinforced 5052Al-based composites with good surface morphology and different diffusion layer thicknesses were successfully prepared using hot-press sintering and annealing, which were subsequently characterized by XRD, SEM, EBSD, micropillar compression, and nano-indentation. The EBSD tests indicate that the  $\text{Al}_{0.6}\text{CoCrFeNi}$  high-entropy alloy has a dual-phase crystal structure with the presence of both FCC and BCC phases inside, and the internal grain size is significantly higher than that of the matrix. Subsequently, the mechanical property mapping images of the particle-diffusion layer-matrix region on the composite surface were obtained using the NanoBlitz 3D method in the nanoindentation experiments. And based on the particle and matrix mechanical property parameters obtained by nanoindentation experiments, they were fitted into different mathematical models to obtain the hardness and elastic modulus of the composite. As a result, the correlation was found to be linear, and the slope of the fitted straight line increased gradually with the prolongation of the annealing time. In conclusion, it is evident from the comparison of the results of mathematical model fitting of mechanical property parameters with the results of macroscopic mechanical property tests that the P. G. Klemens model exhibits an excellent fitting effect on the macro-microscopic mechanical properties of particle-reinforced aluminum matrix composites compared with other models such as the rule of mixtures.

## 1. Introduction

Aluminum matrix composites (AMCs) offer high specific strength, high specific stiffness, good wear and fatigue resistance, excellent dimensional stability, electrical and thermal conductivity while maintaining light weight. Therefore, it is widely used in engineering and structural fields, such as automotive manufacturing, aerospace, defense and military, and electronic packaging [1,2]. Additionally, aluminum matrix composites are categorized into continuous fiber-reinforced, discontinuously reinforced, and laminated composites based on reinforcement [3]. Discontinuous reinforcement primarily consists of short fibers, whiskers, and particles [4], while continuous fiber reinforcement, such as continuous carbon fiber, is currently one of the reinforcements

that possess high tensile strength while maintaining the lowest density [5]. Unfortunately, such materials present complicated preparation processes at high costs, which prevent mass production. Reinforcement in laminated composites enhances the mechanical properties of AMCs by hindering the internal crack expansion and controlling the stress concentration at the crack tip of the composite through interfacial delamination and fracture deflection [6]. Nevertheless, during tensile or compression tests, stresses usually accumulate at the location of the reinforcement-matrix interface due to the irregularity of the reinforcement edges, which eventually leads to the failure and fracture of the composite. Notably, mechanical property anisotropy exists within continuous fiber-reinforced and laminated AMCs, which further restricts their scope of application. Besides, whisker-enhanced AMCs are also

\* Corresponding author.

\*\* Corresponding author.

E-mail addresses: [yuanyekingfly@163.com](mailto:yuanyekingfly@163.com) (Z. Yuan), [yuyuan@licp.acs.cn](mailto:yuyuan@licp.acs.cn) (Y. Yu).

complicated to prepare and costly, resulting in a limited scope of application and research. In comparison with the above-mentioned reinforcements, short fibers and particles are broadly employed as reinforcements in composite materials for their low cost, simple preparation process, and outstanding overall mechanical properties [7]. The short fiber reinforcement can significantly increase the wear resistance [5], tensile strength, and creep resistance [8] of AMCs while notably improving the anti-fatigue life of the material [9]. Nevertheless, in practical applications, short fiber-reinforced AMCs are prone to defects of poor plasticity and toughness, which means seeking ideal reinforcement has become the top priority of numerous scholars. In combination with previous research, it is found that particle-reinforced aluminum matrix composites (PRAMCs) have a broader development prospect since their mechanical properties are isotropic and possess favorable plasticity and toughness coordination at the same time.

With the concept of high-entropy alloy (HEA) proposed by Yeh et al. [10,11], it has attracted extensive attention from scholars at home and abroad because of its high strength, high hardness, good thermal stability, and excellent combination of strength and ductility. HEA generally consists of 5–13 elements, and the content of elements is between 5 and 35%. The outstanding performance mainly originates from its four core effects, i.e., high entropy, severe lattice distortion, slow diffusion, and cocktail effect [11]. The  $\text{Al}_x\text{CoCrFeNi}$  system is one of the earliest studied HEA systems, and the theoretical research has been relatively well established. Notably, the  $\text{Al}_x\text{CoCrFeNi}$  HEA exhibits highly elevated thermal stability in most instances, except for the formation of the  $\text{NiCoCr}$  phase under certain specific conditions [12,13]. Besides,  $\text{Al}_x\text{CoCrFeNi}$  HEA has three different crystal structures (i.e., single FCC phase ( $x \leq 0.4$ ), BCC + FCC phase ( $0.4 < x \leq 0.9$ ), and single BCC phase ( $0.9 < x \leq 2$ )) based on Al element content [2,14]. Li et al. [15] prepared  $\text{Al}_{0.8}\text{CoCrFeNi}$   $\text{HEA}_p/5083\text{Al}$  composites by stirring friction processing. They found that the average microhardness (125.7 HV<sub>0.2</sub>) and Young's modulus (102.4 GPa) of the composites were 56.1% and 16.2% higher than those of 5083Al, respectively. Furthermore, the high-entropy alloy particles maintain good thermal stability during multi-stir friction processing without generating new phases internally. More importantly, Liu et al. [16] found that the yield strength (137 MPa) of composites with the presence of the diffusion layer between  $\text{HEA}_p$  and the matrix was about 42% higher than that of non-diffusion layer composites while preparing  $\text{AlCoCrFeNi}/\text{Al}$  matrix composites using the discharge plasma sintering process. It is demonstrated that the well-bound interfacial effect between  $\text{HEA}_p$  and the matrix can further enhance the mechanical properties of the composites.

In the previous study [17], the growth of diffusion layer thickness of  $\text{Al}_{0.6}\text{CoCrFeNi}/5052\text{Al}$  composites prepared by hot-press sintering under different annealing conditions and its effect on the macroscopic mechanical properties were explored, while a profound analysis of the internal microscopic mechanical properties was absent. In this paper, the crystal structure and mechanical properties of certain regions of  $\text{Al}_{0.6}\text{CoCrFeNi}/5052\text{Al}$  composites with different diffusion layer thicknesses and individual  $\text{HEA}_p$  positions are studied using a combination of focused ion beam etching deposition systems (FIB), electron backscatter diffraction analysis (EBSD), and nanoindentation. Subsequently, combining the experimentally obtained micromechanical property parameters with mathematical models against the results of room temperature uniaxial compression and microhardness tests, an attempt was made to establish a link to the macro-micromechanical analysis of PRAMCs. However, conventional nanoindentation techniques are commonly applied for testing the mechanical properties of non-uniform microstructures at the micron and nanoscale, which can hardly characterize the distribution of mechanical properties in the diffusion layer region of composites [18]. It can be perfectly solved by obtaining the mechanical property mapping in the microstructure region of the composites based on high-speed indentation mechanical property imaging (NanoBlitz 3D method). Zhang et al. [14] obtained Young's modulus growth trend of  $\alpha\text{-AlFeMnSi}$  alloy by the NanoBlitz 3D method, which is

approximately similar to the calculated values derived from the first-principle calculation based on density functional theory (DFT), and some of the measured values are also within the range of the calculation of the DFT method. In addition, Chen et al. [19] yielded the average hardness (11 GPa) and average Young's modulus (219.2 GPa) of  $\text{AlTiVMoNb}$  refractory HEA coatings prepared by the laser melting method by the NanoBlitz 3D method as well. The experimental results are similar to those of the stress-strain method and the Voigt-Hill method in that the hardness and Young's modulus not only follow the same trend but also exhibit errors of about 7%.

## 2. Experimental procedures

### 2.1. Materials preparation

At the present work, commercial  $\text{Al}_{0.6}\text{CoCrFeNi}$   $\text{HEA}_p$  ( $\overline{D_p} = 46.1\mu\text{m}$ ) and commercial 5052Al ( $D_m \leq 48\mu\text{m}$ ) powder were used for the reinforcement and matrix, respectively, and the powder chemical composition is shown in Table 1. The blended powders were obtained by mechanical ball milling in a vacuum environment by loading stainless steel milling balls and powders with a mass ratio of 10:1 into a planet horizontal ball mill. The mixed powders were placed in a vacuum hot-pressing furnace and sintered at 823 K for 1 h to obtain  $\text{HEA}_p/\text{Al}$  composites. (It should be noted that graphite paper is required between the powder and the mold to prevent the composite from bonding with the mold during the hot pressing-sintering process, which would make it difficult to remove the specimen and even damage the mold.) After sintering, the specimens were put into a program-controlled electric resistance furnace for heat treatment and removed after holding at 773 K for 8 h, 24 h, and 96 h, respectively, and cooled to room temperature in atmospheric conditions [17]. The schematic diagram of the composite preparation and the specific experimental parameters are shown in Fig. 1.

### 2.2. Material characterization

A  $10\text{mm} \times 10\text{mm}$  bulk specimen was processed from the annealed  $\text{HEA}_p/\text{Al}$  composite using an electric discharge wire cutting machine for subsequent testing and microscopic morphological observation. The nanoindenter was setting to a load of 1.5 mN, and 6400 nanoindentation test points were uniformly distributed around a single high-entropy alloy in composite with different annealing times in an area of  $120\mu\text{m} \times 120\mu\text{m}$  using the NanoBlitz 3D method (KLA iMicro Instrument, USA), respectively. A diamond Berkovich indenter was used in displacement-controlled mode for the experiments, and the indentation depth was  $\sim 100$  nm and the distance between two indentations was  $1.5\mu\text{m}$ . Micropillars were prepared using a focused ion beam etch deposition system (FIB, Helios 600, USA) by concentric circular milling patterns at 30 KV/5 nA using  $\text{Ga}^+$  ion beams. Remarkably, the  $\text{Ga}^+$  beam current should be reduced to 50 pA when polishing the surface of the micropillar to minimize damage to the surface. Eventually, the diameter of the micropillar is about  $0.5\text{--}2\mu\text{m}$ , with an aspect ratio of 3:1. Micropillar compression experiments were performed on a nanoindenter (Hysitron Ti950, USA) with a flat diamond tip. The experiments were carried out in displaced menstruate-controlled mode at a constant prescribed strain rate of 5 nm/s and unloaded after the micropillar fracture at an unloading rate of 50 nm/s. X-ray diffraction analysis (XRD, NASDAQ: BRKR, D8 Advance, Germany) was used to analyze the possible phases of the  $\text{HEA-Al}$  composite after annealing treatment. Scanning electron microscopy (SEM, Hitachi, S-4800, Tokyo) was used to observe the microscopic morphology of the composite and the growth of the diffusion layer thickness. Samples for microstructural observation and nanoindentation tests are mechanically ground and polished using  $\text{SiO}_2$  suspension.

**Table 1**

The chemical composition of powders.

Material	Element						
	Co	Cr	Fe	Ni	Mg	Si	Al
Al <sub>0.6</sub> CoCrFeNi (at.%) 5052Al(wt.%)	21.7 –	21.7 0.15–0.35	21.7 ≤0.4	21.7 –	– 2.2–2.8	– ≤0.2	13.2 Bal.

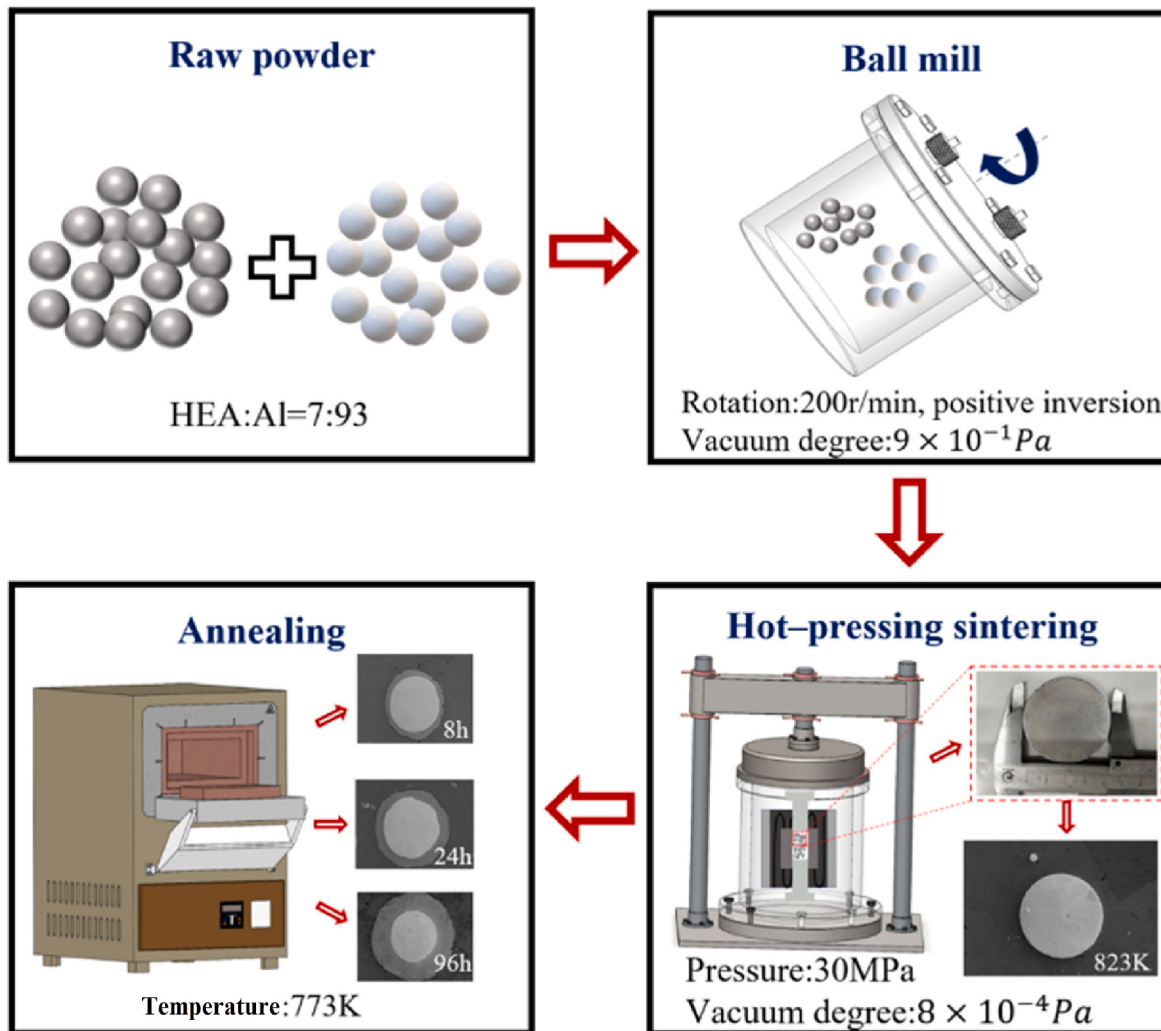


Fig. 1. The schematic diagram of HEA/Al composite preparation.

### 3. Results

#### 3.1. XRD analysis

Fig. 2 shows the X-ray diffraction images of the Al<sub>0.6</sub>CoCrFeNi HEAp/5052Al matrix composites prepared by hot-press sintering and annealing. From the figure, it is evident that the intensity of the HEA peaks in the annealed composites increased, and the diffraction peaks of Al<sub>9</sub>Co<sub>2</sub>-, Al<sub>13</sub>Co<sub>4</sub>-, and Al<sub>18</sub>Cr<sub>2</sub>Mg<sub>3</sub>- type intermetallic compounds (IMCs) were found. Based on previous investigations [9,20], we can conclude that the Al<sub>9</sub>Co<sub>2</sub>- and Al<sub>13</sub>Co<sub>4</sub>-type IMCs may have been generated by the diffusion of other metallic elements in the HEAp instead of the Co elements, which eventually resulted in the formation of Al<sub>9</sub>(CoCrFeNiMg)<sub>2</sub> and Al<sub>13</sub>(CoCrFeNi)<sub>4</sub> IMCs. The previous quantitative analysis [17] of diffusion layer elements confirms that the formation mechanism of Al<sub>18</sub>Cr<sub>2</sub>Mg<sub>3</sub>-type IMCs is similar to that of Al-Co-type IMCs.

#### 3.2. Micromorphological analysis

Fig. 3 reveals the microscopic morphology of the composites under different annealing times. With the prolongation of the annealing time, a diffusion layer gradually formed at the interface between Al<sub>0.6</sub>CoCrFeNi HEAp and the 5052Al matrix, and its thickness progressively increased. Then, the thickness of the diffusion layer formed along the interface from the HEAp to the matrix becomes uniform in different directions (Fig. 3a–d) and eventually creates a regular circular interface between the HEAp and the matrix. However, when the annealing time was prolonged up to 96 h, certain adjacent HEAp in the composites interfered with the diffusion layer, and prevented further growth, while minor particles even diffused to complete disappearance, as shown in Fig. 3d. The element diffusion rate and the thickness of the diffusion layer in the composites can be obtained by combining the Arrhenius equation with parabolic growth expressions of the diffusion layer [21,22].

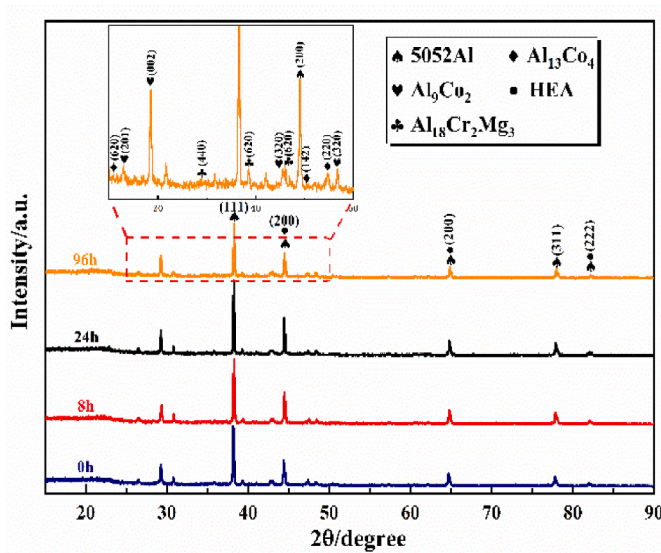


Fig. 2. XRD images of composites with different annealing times.

$$D = D_0 \exp\left(-\frac{Q}{RT}\right) \quad (1)$$

$$y^2 = Dt \quad (2)$$

Where  $D$  and  $D_0$  are the elemental diffusion coefficient and frequency factor, respectively;  $Q$  is the diffusion activation energy; and  $R$  is the gas constant, generally regarded as  $R = 8.314 \text{ J} \cdot \text{mol}^{-1} \text{K}^{-1}$ ;  $T$  is the processing temperature in  $\text{K}$ ;  $y$  is the diffusion layer thickness; and  $t$  is the annealing time. According to the previous work [17], there was no

diffusion layer formation at the interface between HEA<sub>p</sub> and matrix when the HEA<sub>p</sub>/Al composites were annealed at lower temperatures, despite the extension of the annealing time. Based on the above equation, the diffusion layer thickness ( $y$ ) is principally associated with  $D_0$ ,  $Q$ , and  $T$ . Normally,  $5 \times 10^{-4} \text{ m}^2 \cdot \text{s}^{-1} \leq D_0 \leq 5 \times 10^{-6} \text{ m}^2 \cdot \text{s}^{-1}$ , hence the frequency factor can be almost negligible on the elemental diffusion coefficient. Consequently, the material can overcome the energy barrier ( $\Delta G_m$ ) and leap only at a sufficiently high processing temperature, i.e., when the internal atoms acquire sufficient diffusion activation energy ( $Q$ ), enabling the diffusion of elements in the composite. It is notable that thermodynamic motions of uniform materials have been found to be disordered internally in previous studies, i.e., interatomic leap ranges are small and completely irregular, which contributes to the non-directional orientation of internal element diffusion. Therefore, a high concentration gradient (i.e., chemical potential gradient) exists between the HEA<sub>p</sub> and Al matrix, which is the driving force for the directional diffusion of elements from the higher concentration to the lower region [15], and the diffusion direction is opposite to the positive direction of the concentration gradient, which also provides evidence for the formation of IMCs in the diffusion layer. In addition, it is evident from Fig. 3b<sub>1</sub>-d<sub>1</sub> that the diffusion layer between the particles and the matrix in the composite gradually transformed from one to two layers as the annealing time prolonged and eventually turned into a one-layer diffusion layer once again at the annealing time of 96 h. It may be related to the fact that certain elements with greater diffusion rates occupy diffusion channels in the interface at the beginning of the annealing treatment, which prevents other elements from diffusing. From Eq. (2), it is known that the diffusion distance among elements with different diffusion rates gradually emerges as differences over the same time, thus a delamination phenomenon appears in the diffusion layer. However, with the prolongation of the annealing time, the elements were completely diffused in HEA, and diffusion distances were gradually approached, which consequently resulted in the reappearance

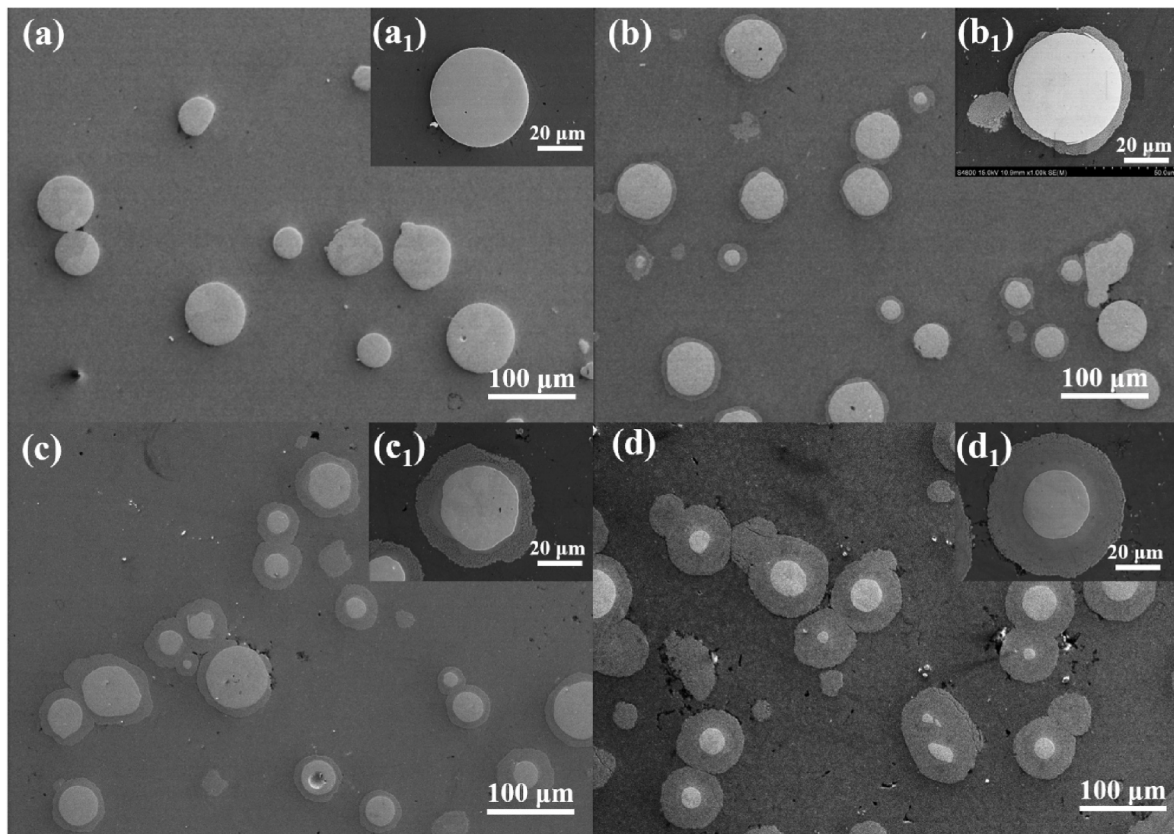


Fig. 3. Micromorphology of composites with different annealing times (a) (a<sub>1</sub>) 0 h, (b) (b<sub>1</sub>) 8 h, (c) (c<sub>1</sub>) 24 h, (d) (d<sub>1</sub>) 96 h.

of the one-layer diffusion pattern.

### 3.3. Electron back scatterer diffraction analysis

The electron backscattering diffraction analysis (EBSD) was performed on selected regions and individual high-entropy alloy particles in the Al<sub>0.6</sub>CoCrFeNi HEAp/5052Al composites annealed at 773 K 8 h, respectively, and the results are shown in Figs. 4 and 5. From Fig. 4a and 5a, the grain size distribution in the matrix varies widely, and there are smaller grains near the HEAp, with an average grain size of about 13.12 μm (Fig. 4c). In contrast, the grain size inside the high-entropy alloy is significantly higher than that of the matrix, but the range of variation in dimensions is smaller. The appearance of massive, small-sized grains in the matrix near the HEAp can be investigated from several angles. Above all, the obvious difference in thermal expansion coefficients between the HEAp and the matrix during the annealing treatment led to the formation of higher-density dislocations, which sped up the particle-stimulated nucleation (PSN) and helped the grains in the matrix recrystallize. In contrast, the distributed HEAp hinders the grain boundary motion through the Zener drag effect, which slows down the grain growth [23,24]. As for the phase distribution patterns (Fig. 4b and 5b), the matrix consists of only face-centered cubic phase (FCC phase), while the presence of both FCC phase (red region) and body-centered cubic phase (BCC phase) (green region) can be observed inside the HEAp, where the FCC phase in the high-entropy alloy was mainly enriched with Co, Cr, and Fe elements, and the BCC phase was mainly enriched with Ni and Al elements [25]. It can demonstrate that Al<sub>0.6</sub>CoCrFeNi is a dual-phase high-entropy alloy containing both FCC and BCC phases [2, 14] and can illustrate that although a diffusion layer is formed between the HEAp and the matrix due to interdiffusion during annealing, its interior still maintains good thermal stability without new phase generation. From the pole figures (Fig. 4e–f, and Fig. 5e–f), it can be found that the internal pole density of the composite is relatively low and there is no obvious preferred orientation, while the pole density of the BCC phase in the HEAp reaches 20.08; hence, there may be a preferred orientation in the <100> and <111> directions.

### 3.4. Mechanical property mapping

It was reported that [26] if the spatial spacing between two adjacent indentations in nanoindentation experiments is greater than or equal to 10 times the penetration depth, then the interaction during nanoindentation can be eliminated. Moreover, the distance between the two

adjacent indentations obtained by the NanoBlitz 3D method in this paper is 1.5 μm, and the indentation depth is only ~100 nm, so the error caused by interference can be inhibited. The hardness and elastic modulus acquired from the nanoindentation mapping experiment are taken as the Z-axis, and the horizontal and vertical displacements of the indenter are plotted as the X-axis and Y-axis to obtain the mapping images of the mechanical property parameters for the whole regions, including the HEAp, the diffusion layer, and the matrix, as shown in Fig. 6. The metallographic microscopy images of the tested regions of the composites with different annealing times are shown in Fig. 6a1–c1, respectively. From Fig. 6a–f, it can be observed that the indentation test locations can be clearly divided into three parts according to the different colors: the HEAp, the diffusion layer (DL), and the matrix, corresponding to the three-layer structure in the SEM image in the composites (Fig. 3). As the annealing time was extended from 8 h to 96 h, the area of the HEAp gradually decreased while that of the diffusion layer progressively increased, where the HEAp area corresponded to the maximum values of the elastic modulus and hardness of the composites, with the values decreasing by 21.9% and 21.5%, respectively. However, mechanical properties varied slightly after annealing treatment in the matrix. Probably explained by the fact that the HEA serves as a diffusion source and its internal elements continuously diffuse into the particle-matrix interface to form a diffusion layer, which reduces the concentration of elements in the HEA, thus resulting in a dramatic decrease of the mechanical properties at its edges. In contrast, 5052Al alloy is a non-heat-treatable strengthening alloy [27], so annealing treatment influences it slightly. The previous study [17] found that as the annealing time was extended beyond 8 h, the diffusion layer thickness continued to increase while the mechanical properties became progressively worse, which can be attributed to the following reasons in combination with the mapping images of mechanical properties obtained by the NanoBlitz 3D method: Firstly, the annealing treatment eliminates the residual stresses formed during the preparation as well as the processing of the composites, and consequently, the internal hardness is reduced [28]; Additionally, during the annealing process, interdiffusion between the HEAp and the matrix occurred. As shown by the yellow arrows in Fig. 6e–f, the different rates of elemental interdiffusion between the two led to the formation of Kirkendall holes at the matrix side of the diffusion layer [29], which destroyed the metallurgical bonding interface and decreased the overall mechanical properties of the composite [30]. On the other hand, in comparison with the SEM images of the composites without annealing treatment, small, sporadic, and irregularly distributed pores (as indicated by the green arrows in

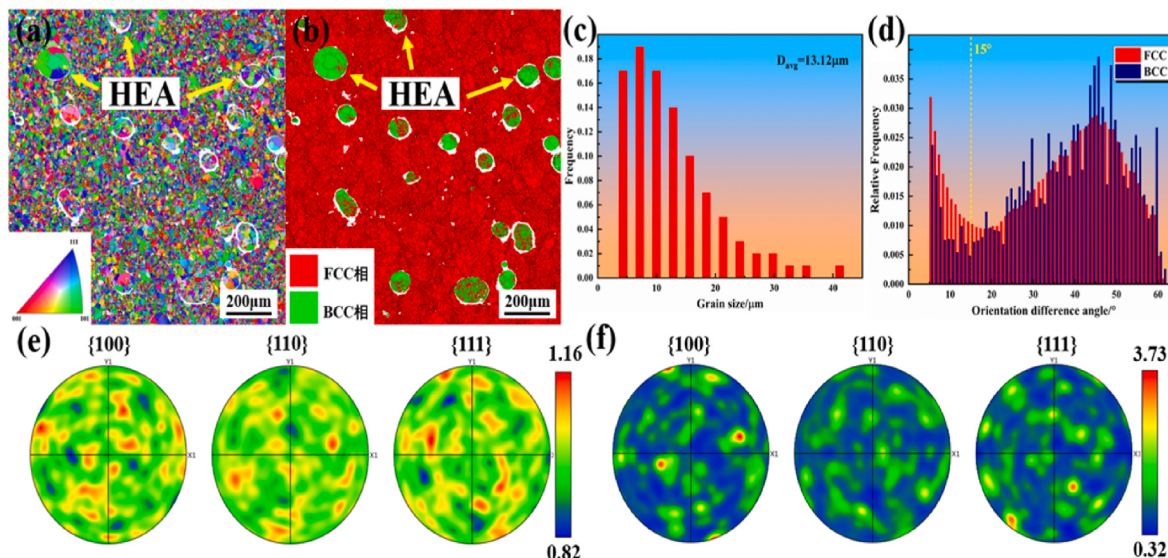


**Fig. 4.** EBSD analysis of composites (a)(c) grain size distribution (b)(d) phase distribution (e) and (f) are the polar figures of the FCC and BCC phases, respectively.

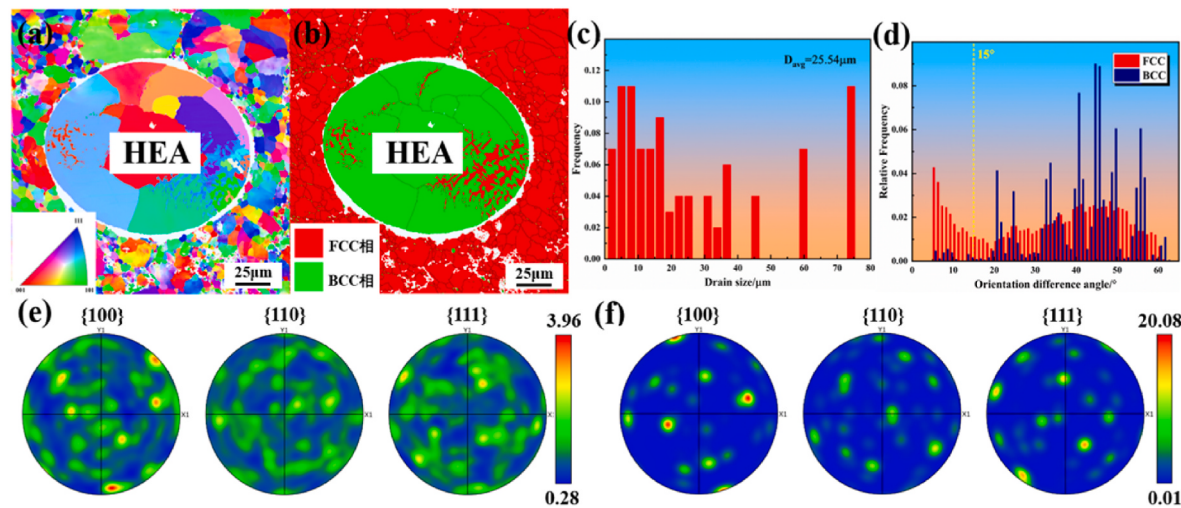


**Fig. 5.** EBSD analysis of certain particles in composite (a)(c) grain size distribution (b)(d) phase distribution (e) and (f) are the polar figures of the FCC and BCC phases, respectively.

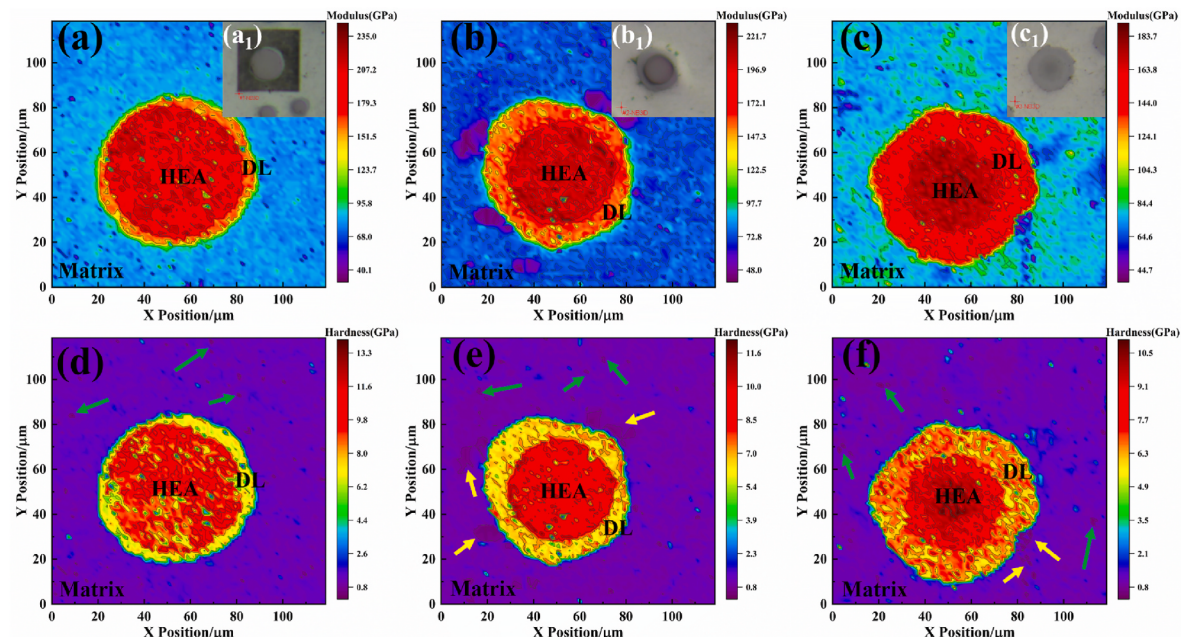


**Fig. 6.** Mapping images of elastic modulus and hardness of composites at different annealing times (a) (d) 8 h, (b) (e) 24 h, (c) (f) 96 h, where (a<sub>1</sub>), (b<sub>1</sub>), and (c<sub>1</sub>) are the locations of indentation of composites at different annealing times, respectively.

**Fig. 6d–f** were found in the matrix, and the number of pores tended to increase as the annealing time extended; Combinations of the above factors may be contributing to the progressive decrease of the overall mechanical properties of the composite with extended annealing time, despite the increasing thickness of the diffusion layer.

### 3.5. Micropillar compression experiments

Micropillars with diameters of approximately 0.5–2 μm were prepared using FIB in the diffusion layer of Al<sub>0.6</sub>CoCrFeNi HEA<sub>p</sub>/Al composites with an annealing time of 24 h. Experimental results of micropillar preparation and compression are shown in Fig. 7. Interestingly, Frick et al. [31] revealed that the deformation of micropillars of different diameters was homogeneous when loads were applied and was independent of the applied strain scale, meaning that differently sized micropillars can be used for comprehensive analysis of the

characteristics in the diffusion layer of composites. In Fig. 7b, when the strain of the composite reached 3%, the stress-strain relations were no longer linear for all micropillars, but the 0.53 μm diameter and their compressive strain were over 30% at the end of microcompression. Furthermore, yielding emerged in the 1.73 μm micropillar when the applied stress reached 2.6 GPa. However, the yield point of the <1.73 μm micropillars is close to 4 GPa, but the margin of strain mutation and strain hardening is significantly lower than that of the 1.73 μm micropillars. Interestingly, the engineering stress-strain curve is smoother for micropillars >1 μm in diameter before yielding occurs, while smaller ones fluctuate in a small range; the smaller the diameter, the more noticeable it becomes. Since larger-diameter micropillars are more resistant to plastic deformation, the measured stresses are more stable. Basak et al. [1] indicated that yield point in stress-strain curve might not denote the exact critical stress necessary to move a dislocation on slip plane. In contrast, it shows what stress level is required to activate

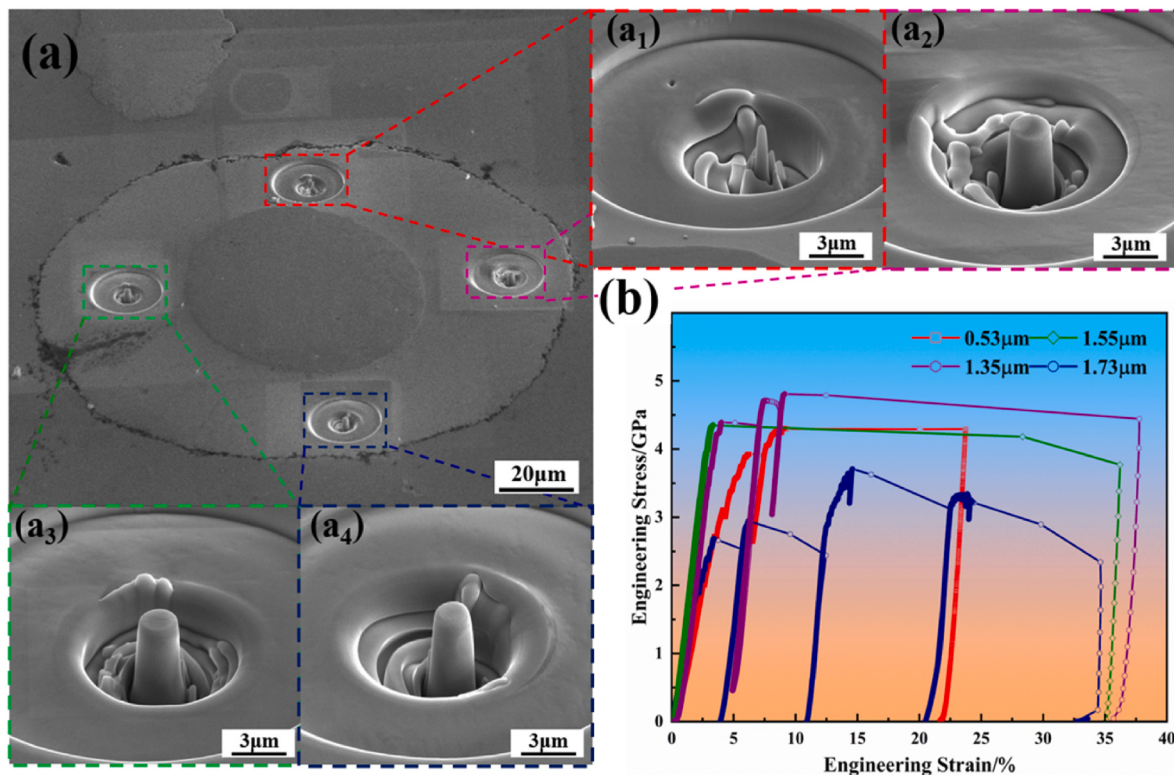


**Fig. 7.** Fabrication and compression experiments on micropillars (a) SEM image of micropillar position (b) engineering stress-strain curves for microcolumn compression (a<sub>1</sub>), (a<sub>2</sub>), (a<sub>3</sub>) and (a<sub>4</sub>) are SEM images of 0.53 μm, 1.35 μm, 1.55 μm, and 1.75 μm micropillars, respectively.

dislocation sources within the pillars, and once the required stress level is reached, the dislocation slip occurs. And as plastic deformation occurs within the composite by slip band formation during compression, the number of slip bands also increases with increasing strain [1]. Specifically, as the displacement of the diamond indenter increases, the strain of the composite begins to show discontinuities, significant bursts, and a dramatic stress reduction. Besides, several strain bursts may occur in the micropillar along with the sharp decrease in stress, and large slip steps can be found on the surface of the micropillar after deformation [31]. Where the elastic deformation period represents the linear increase in load with displacement at the beginning of the loaded experiment; While the plastic deformation period of sudden strain burst occurs as the dislocations move or shear deformation proceeds. Since the diameter and height of the micropillar are both on the micron scale and the overall rate of rapid dislocation movement within the micropillar would be higher than the external loading rate, a sudden strain burst occurs in the stress-strain curve. Additionally, after the first yielding in the composite, slip bands started to appear in the micropillars, and the formation of new slip bands was associated with a significant decrease in stress in subsequent loading [31]. The smaller micropillars also displayed a higher yield strength. Such a “smaller is stronger” size effect in materials at the micron and nanometer scales may be related to dislocation starvation theory [32]. In compression experiments, dislocations in the micropillars can easily escape from the free surface during slip, and their rate could exceed the rate of dislocation proliferation in the composite, which results in a gradual decrease in dislocation density during deformation and even reaches complete dislocation starvation [31]. In this case, plastic deformation can only proceed by excitation of the internal dislocation nucleation through increased loading. However, total starvation of dislocations in large-diameter micropillars is hardly achieved. As the size of the micropillar increases, the residual dislocation interactions within the material become a new source of dislocation, and the resistance to dislocation movement increases. The dominant deformation mechanism here is dislocation movement stress, so the smaller

the micropillar, the higher the yield strength required [31]. In this study, the yield strength of the 0.53 μm pillar was higher than that of the 1.75 μm one but lower than that of the other two pillars, without a “smaller is stronger” sizing effect. This is probably attributable to the more severe damage to the surface of the pillar caused by the Ga<sup>+</sup> beam during the processing. On the other hand, the strain hardening rate of the composite increases significantly at strains of 5–15%, and the yield strength corresponding to the re-emergence of the slip is markedly higher than the initial slip. Interactions between dislocations within the micropillars occur, creating cross-slip, and the slip bands that are created earlier in the dislocation intersection hinder dislocation movement. Besides, dislocation agglomeration occurs at the location of the slip band, so the hardening rate of the material increases.

## 4. Discussion

### 4.1. Analysis of mechanical properties in microscopic areas

Based on previous research [33], the elastic modulus is only related to the elastic deformation of the material, whereas hardness is related to both elastic and plastic deformation. Since the Berkovich diamond indenter was used in the nanoindentation mapping experiments, the hardness and elastic modulus of the composite can be directly calculated by the Oliver and Pharr method [34–36]:

$$H = \frac{L_{max}}{A_{max}} \quad (3)$$

$$\frac{1}{E_r} = \frac{1 - \nu^2}{E} + \frac{1 - \nu_i^2}{E_i} \quad (4)$$

where H is the hardness of the material,  $L_{max}$  is the maximum load reached during the test, A is the contact area determined by the Oliver and Pharr method, and  $E_r$  is previously defined reduced modulus [36]. And  $E$ ,  $E_i$ ,  $\nu$  and  $\nu_i$  are the elastic modulus and Poisson's ratios of the

specimen and indenter, respectively. The elastic modulus and hardness obtained from the nanoindentation mapping were plotted as the horizontal and vertical coordinates, respectively, with the linear fitting of the resulting images, as shown in Fig. 8. From the overall distribution of the experimental data in the plot, it appears that the hardness of the composites at different annealing times follows the same trend as the elastic modulus and that the higher the elastic modulus, the higher the hardness. Furthermore, the hardness and elastic modulus of the specimens with an annealing time of 8 h were higher than the other two specimens, and the data were more discrete. However, when the elastic modulus ranged from 150 to 175 GPa, the H-E values of the specimens annealed for 96 h were more intensive and greater than those of the other two specimens. Perhaps because of a progressive reduction in the difference of element kinds and concentrations between the HEA and the diffusion layer at the annealing time of 96 h, the mechanical property parameters are also gradually approached. Besides, previous studies revealed that the elastic modulus of the material in the nanoindentation test exhibited a linear relationship to hardness, and its slope was the elasticity index ( $I_E = H/E$ ) [37–39]. Its linear relations can be characterized by the following equations [19,33]:

$$H = 0.151 \frac{E}{2(1 + \nu)} \quad (5)$$

Where,  $\nu$  is the Poisson's ratio. In Fig. 8, the hardness of the  $\text{Al}_{0.6}\text{CoCrFeNi}$  HEA<sub>p</sub>/Al composite is similarly linearly related to the elastic modulus, and the slope of the fitted line ( $I_E$ ) gradually increases with prolonged annealing time. The higher  $I_E$  indicates a less ductile material, which is consistent with the results of uniaxial compression tests at room temperature [17]. In this case, the bias of the linear ratio between hardness and elastic modulus may be related to inelastic deformation such as dislocation slips during nanoindentation.

#### 4.2. Analysis of the distribution of mechanical properties

Based on the mechanical properties' histograms of the composites at different annealing times obtained from the nanoindentation mapping images (Fig. 9), it is evident that the hardness and elastic modulus can be divided into three different regions according to the value taken, i.e., corresponding to the HEA<sub>p</sub>, the diffusion layer, and the matrix, respectively. Among them, the elastic modulus and hardness of the matrix vary over a minor range, being close to 75 GPa and 1 GPa, respectively, while the diffusion layer and the particles have a high degree of dispersion at

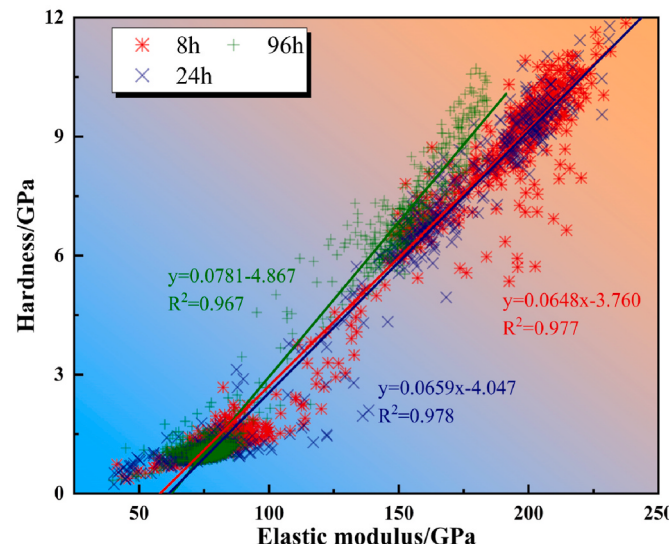


Fig. 8. Hardness-elastic modulus images of composites with different annealing times.

the corresponding locations. Additionally, the mean values of hardness and elastic modulus of the composites for different annealing times were calculated from the mechanical properties histograms and recorded in Table 2. Now, a first-principles calculation based on density functional theory (DFT) is a reliable and effective method for predicting the stability, electronic structure, and mechanical properties of various intermetallic compounds and alloy systems [14]. Zhang et al. [14] and Chen et al. [19] have verified the experimental results of nanoindentation mapping by the DFT method and proved the accuracy of the NanoBlitz 3D method. In this case, the elastic modulus, hardness, and Poisson's ratio of the material can be calculated according to the following equations:

$$E = \frac{9BG}{3B + G} \quad (6)$$

$$H = 0.151G \quad (7)$$

$$\nu = \frac{3B - 2G}{2(3B + G)} \quad (8)$$

Where B and G are the bulk and shear moduli calculated by the Voigt-Reuss-Hill method (VRH), respectively, and  $\nu$  is the Poisson's ratio [14,19,40]. In a previous investigation [41], the elastic constants of  $\text{Al}_x\text{CoCrFeNi}$  HEA with different Al elemental contents (x) were calculated and analyzed, and the results are shown in Table 3. By substituting the values in Table 3 into equations (6)–(8) and comparing the results with the elastic modulus and hardness of the  $\text{Al}_{0.6}\text{CoCrFeNi}$  high-entropy alloy obtained by the NanoBlitz 3D method, the experimental values are within the predicted values of the DFT method. Consequently, the experimental results obtained from nanoindentation mapping can be used as microscopic mechanical property parameters for the composite.

#### 4.3. Macro-micro mechanical property modeling analysis

For investigating the relations between the macro- and micro-mechanical properties of  $\text{Al}_{0.6}\text{CoCrFeNi}$  HEA<sub>p</sub>/5052Al matrix composites, the mechanical property parameters obtained from nanoindentation mapping were fitted by a mathematical model and compared with the results of room temperature uniaxial compression and microhardness tests [17], which resulted in the well-fitted mathematical model. Prior research reveals that the straight and curved parts of the uniaxial compression curve of a composite represent the elastic and plastic deformation of the material, respectively. And the slope of the straight part (i.e., the elastic modulus of the composite) can be calculated from the equation [42].

$$E = \frac{\sigma}{\epsilon} \quad (9)$$

Where  $E$  is the elastic modulus in GPa;  $\sigma$  represents the engineering stress in GPa [43]; and  $\epsilon$  represents the engineering strain. The microhardness can be expressed by the following equation [44]:

$$HV_{0.2} = 1.8544 \frac{F}{d^2} \quad (10)$$

Where  $HV_{0.2}$  is the Vickers hardness and the unit is  $\text{kg} \cdot \text{mm}^{-2}$  [45,46],  $1\text{kg} \cdot \text{mm}^{-2} = 9.80665\text{N} \cdot \text{mm}^{-2} = 9.80665 \times 10^{-3}\text{GPa}$  [47];  $F$  is the applied load;  $d$  is the average value of the measured diagonals of the indentation mark in mm. Therefore, the microhardness can also be expressed by the following equation [47]:

$$HV = (1.891 \times 10^{-4}) \frac{F}{d^2} \quad (11)$$

Where  $HV$  is the Vickers hardness and the unit is GPa. From these equations, the results obtained from room temperature uniaxial

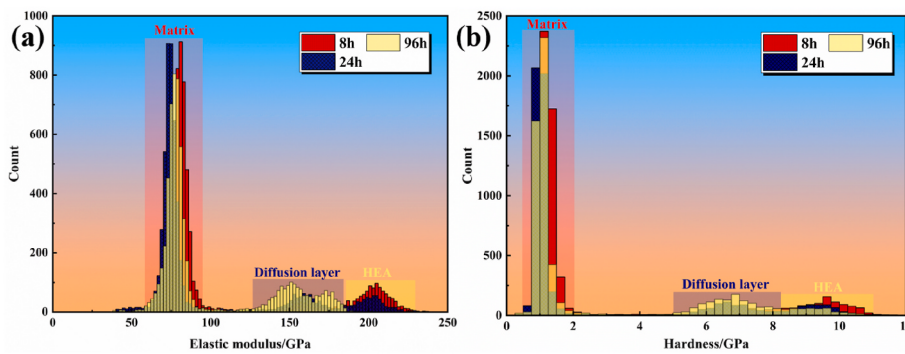


Fig. 9. Mechanical property histograms of annealed composites (a) elastic modulus, (b) hardness.

**Table 2**  
Parameters of mechanical properties for annealed composites.

Mechanical property parameter		Annealing time		
		8 h	24 h	96 h
Elasticity modulus/GPa	HEAp	227.02	220.52	182.24
	Diffusion layer	166.76	168.98	158.54
	Matrix	83.99	73.04	76.83
Hardness/GPa	HEAp	11.27	10.76	9.88
	Diffusion layer	8.11	7.70	7.91
	Matrix	1.24	1.10	1.01

**Table 3**  
Polycrystal elastic moduli for Al<sub>x</sub>CoCrFeNi [41].

x	crystal structure	B/GPa	G/GPa	B/G	E/GPa	$\nu$	H/GPa
0	FCC	207	110	1.88	280	0.275	16.6
0.3	FCC	196	96	2.04	248	0.289	14.5
0.5	FCC	190	89	2.13	231	0.297	13.4
1.0	FCC	183	76	2.40	201	0.317	11.5
1.0	BCC	178	78	2.29	204	0.309	11.8
1.3	BCC	170	78	2.17	203	0.301	11.8
1.5	BCC	167	78	2.13	202	0.297	11.8
2.0	BCC	159	77	2.06	199	0.291	11.7

compression and Vickers hardness experiments [17] (Fig. 10a and b) at different annealing temperatures can be transformed and used as macroscopic mechanical property parameters for the HEAp/Al composites.

Then, mathematical models fit the macro- and micro-mechanical property parameters to look for a connection between the two. In numerous mathematical models, the rule of mixtures (ROM) is probably the simplest way to approach the mechanical properties of particle-reinforced metal matrix composites [48]. In particular, the Voigt and Reuss models based on the assumption of equal strain and stress are more widely used [49]. Besides the above-mentioned ROM, Paul's, Maxwell's, and P. G. Klemens' models are commonly used to fit the mechanical properties of composites [19,49,50]. The elastic modulus of the particles and matrix in the composite obtained from nano-indentation tests was inserted into five mathematical models such as Voigt, Reuss, Paul, Maxwell, and P. G. Klemens' models to yield the elastic modulus of the composite and marked as follows:

$$E_1 = E_P V_P + E_M V_M \quad (11)$$

$$E_2 = \frac{E_P \times E_M}{E_P V_P + E_M V_M} \quad (12)$$

$$E_3 = E_M \frac{E_M + (E_P - E_M)V_P^{2/3}}{E_M + (E_P - E_M)V_P^{2/3}(1 - V_P^{1/3})} \quad (13)$$

$$E_4 = E_M \left[ \frac{1 + 2 \frac{E_M}{E_P} - 2V_P \left( \frac{E_M}{E_P} - 1 \right)}{1 + 2 \frac{E_M}{E_P} + 2V_P \left( \frac{E_M}{E_P} - 1 \right)} \right] \quad (14)$$

$$E_5 = E_M(1 - V_P) + E_P V_P - \frac{1}{3}(1 - V_P)V_P \frac{(E_M - E_P)^2}{E_M(1 - V_P) + E_P V_P} \quad (15)$$

Where  $E_M$ ,  $V_M$ ,  $E_P$  and  $V_P$  represent the elastic modulus and volume fraction corresponding to the matrix and HEAp, respectively. The hardness of the composite can also be fitted by employing the five models mentioned above, and the results of the mathematical model fitting are recorded in Fig. 10 along with the experimental values obtained from the macroscopic mechanical properties tests. In Fig. 10c and d, mechanical property parameters calculated by the Reuss model are more than 50% higher than those fitted by other mathematical models and deviate severely from the predicted range. Despite the same tendency of the fitted curves of the Voigt, Paul, and Maxwell models, significant inaccuracy was observed among the experimental values. Notably, the hardness and elastic modulus, calculated by the P. G. Klemens' model, not only have the same trend of variation as the macroscopic mechanical property parameters but also exhibit lower margins of error. Particularly, the experimental and fitted values of macro- and microhardness almost exactly coincide with each other, which permits the use of the P. G. Klemens' model as a reference for the prediction of the macro- and micro-mechanical properties of Al<sub>0.6</sub>CoCrFeNi HEAp/5052Al matrix composites. Explanations for the overestimated values of the mathematical model can be considered in the following terms: Above all, the mathematical model assumed that the reinforcement particles are ideal without angles, smooth, and uniform in particle size, and that the particles are uniformly distributed in the matrix, which is almost impossible for realization in the experiment. Secondly, interfacial failure and the porosity effect on the mechanical properties of the material are not considered. Furthermore, the role of the diffusion layer between HEAp and the Al matrix is ignored. During the annealing treatment, a diffusion layer is formed in the region of the interface between the HEAp and the matrix due to the diffusion of elements, and the mechanical properties are intermediate between the particles and the matrix. Besides, after annealing for sufficiently prolonged periods, where the particles disappear completely, only the presence of the diffusion layer can be observed, so the impact on the mechanical properties of the composite cannot be ignored. On the other hand, the elastic modulus in room-temperature uniaxial compression experiments represents the resistance of the specimen to elastic deformation [51], while the elastic modulus obtained by nanoindentation is primarily related to the strength of the interatomic bonds in the composite [26].

## 5. Summary and conclusions

In this work, hot-press sintering, annealing in a resistance furnace,

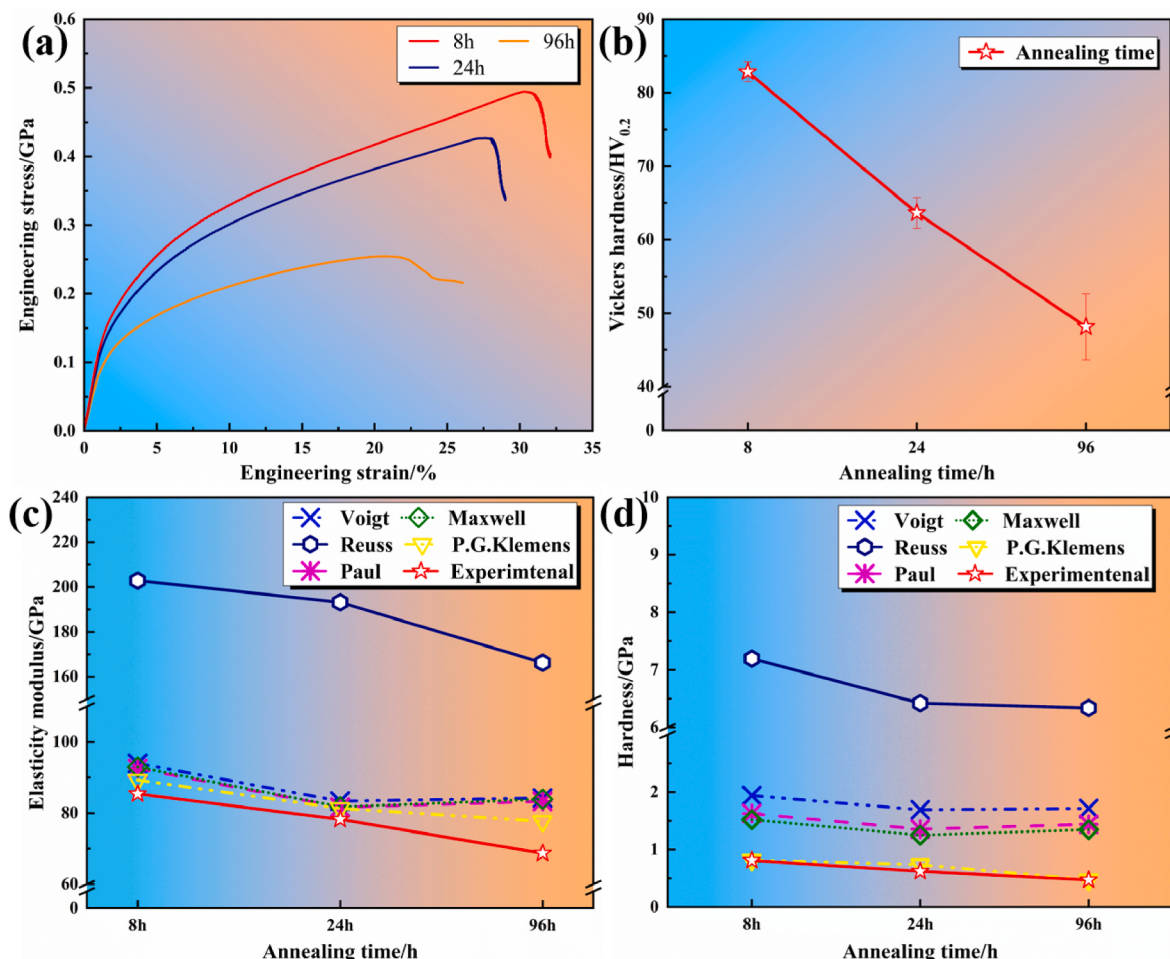


**Fig. 10.** Mechanical parameters of HEAp/Al composites (a) uniaxial compression at room temperature (b) Vickers' hardness (c) and (d) are mathematical models for elastic modulus and hardness, respectively.

and obtaining composites with various diffusion layer thicknesses produced  $\text{Al}_{0.6}\text{CoCrFeNi}$  HEAp/5052Al matrix composites with good surface morphology and no diffusion layer. Furthermore, the surface micromorphology, crystal structure, and micromechanical properties of the composites were observed and analyzed by SEM, EBSD, nano-indentation mapping experiments, and micropillar compression experiments, and the conclusions are obtained as follows:

- (1) During the annealing treatment, the concentration gradient between the HEAp and the matrix serves as a driving force for the diffusion of the elements between them, which results in a gradual increase in the thickness and uniformity in the width of the diffusion layer in all directions outwards along the particle and eventually generates a regular circular diffusion layer at the interface. While assuming that the annealing time is extended indefinitely, the HEAp may disappear completely due to elemental diffusion, and only the diffusion layer and matrix can be observed in the composite.
- (2) Both FCC and BCC phases can be observed within the high-entropy alloy, and the grain size is significantly higher than that of the matrix, which contains only the FCC phase. The presence of numerous small-sized grains in the matrix near the HEAp is probably due to the particle-stimulated nucleation that allows recrystallization into the matrix, while the Zener drag effect limits grain boundary movement and resists the growth of recrystallized grains.

- (3) The elastic modulus obtained in the nanoindentation mapping experiments is linearly plotted against hardness, and the slope of the fitting line ( $H/E$ ) gradually increases with increasing annealing time, with higher values indicating poor ductility of the composite. Presumably, as the annealing time increases, factors such as Kirkendall holes formed on the matrix side of the diffusion layer due to diffusion and holes within the matrix appear to weaken the mechanical properties more than the ability of the diffusion layer thickness to increase the mechanical properties, so the overall mechanical properties of the composite gradually decrease.
- (4) Micropillar compression consists of an elastic deformation stage and a plastic deformation stage with a strain burst. As the loading increases, dislocations within the small-diameter micropillar escape from the free surface, resulting in a decrease in density, eventually reaching an entirely deprived state where the plastic deformation can only continue by increasing the load to stimulate dislocation nucleation. Whereas dislocation interactions within the residual large diameter micropillar form a new source of dislocation, the dislocation movement stresses become the dominant deformation mechanism, thus the “smaller the stronger” size effect may occur.
- (5) Since the mathematical models are assumed to be ideal and ignore the plastic deformation of the matrix, the shape and spatial distribution of the HEAp, and the presence of diffusion layers, the results of the mathematical models for the mechanical properties of the composites are generally higher than the experimental

values. Compared with the rule of mixtures, Paul's model, and Maxwell, the hardness and elastic modulus of the composites derived from the P. G. Klemens model not only show the same trend as the macroscopic mechanical properties but also have relatively low tolerances.

## CRediT authorship contribution statement

**Zhanwei Yuan:** Resources, Project administration, Funding acquisition, Supervision. **Zhe Ma:** Investigation, Methodology, Visualization, Writing – original draft. **Hao Zhang:** Supervision. **Kai Wang:** Investigation, Writing – review & editing. **Yuan Yu:** Supervision. **Shurong Li:** Investigation. **Xuemin Zhang:** Supervision. **Jingyi Wang:** Investigation. **Danli Zhang:** Supervision.

## Declaration of competing interest

The authors declare that they have no known competing financial interests or personal relationships that will affect the reporting in this article.

## Data availability

No data was used for the research described in the article.

## Acknowledgement

The authors are very grateful for the support received from Nature Science Foundation of Shaanxi (No.2021JQ-286), Key research and Development Plan in Shaanxi Province of China (2021GY-211), and Fundamental Research Funds for the Central Universities, CHD (No.300102311403). And thanks for the support received from Youth Innovation Promotion Association CAS (grant numbers 2021423).

## References

- [1] A.K. Basak, A. Pramanik, C. Prakash, Deformation and strengthening of SiC reinforced Al-MMCs during in-situ micro-pillar compression, *Mater. Sci. Eng.* 763 (2019) 9.
- [2] Y.Z. Liu, J. Chen, X.H. Wang, et al., Significantly improving strength and plasticity of Al-based composites by in-situ formed AlCoCrFeNi core-shell structure, *J. Mater. Res. Technol.* 15 (2021) 4117–4129.
- [3] C.Q. Gao, Q.B. Wang, M.Y. Wei, et al., Effects of reinforcement volume fraction on mechanical properties and microstructures of 7075Al matrix composites reinforced by FeCoCrNiAl high-entropy alloy particles, *Metals* 12 (5) (2022) 10.
- [4] J.L. Bucaille, A. Rossoll, B. Moser, et al., Determination of the matrix in situ from stress of a continuous fibre reinforced metal matrix composite using instrumented indentation, *Mater. Sci. Eng.* A369 (1–2) (2004) 82–92.
- [5] W.P. Mu, J.B. Lin, E.Q. Liu, et al., Fabrication of continuous carbon-fibers reinforced aluminum matrix composites and coating evolution during heat treatment, *J. Mater. Res. Technol.* 17 (2022) 1852–1867.
- [6] C.M. Cepeda-Jimenez, M. Pozuelo, J.M. Garcia-Infanta, et al., Influence of the alumina thickness at the interfaces on the fracture mechanisms of aluminium multilayer composites, *Mater. Sci. Eng.* 496 (1–2) (2008) 133–142.
- [7] S.K. Thakur, M. Gupta, Improving mechanical performance of Al by using Ti as reinforcement, *Composites Part A* 38 (3) (2007) 1010–1018.
- [8] J. Olbricht, A. Yawny, M.L. Young, et al., Mechanical and microstructural observations during compression creep of a short fiber reinforced AlMg metal matrix composite, *Mater. Sci. Eng.* 510–11 (2009) 407–412.
- [9] L. Yi, B. Al-Matar, G. Newaz, An investigation on the interface in a NiTi short-fiber-reinforced 6061 aluminum composite by transmission electron microscope, *Metall. Mater. Trans.* 39 (11) (2008) 2749–2759.
- [10] H. Ping-Kang, Y. Jien-Wei, S. Tao-Tsung, et al., Multi-principal-element alloys with improved oxidation and wear resistance for thermal spray coating, *Adv. Eng. Mater.* 6 (1–2) (2004) 74–78.
- [11] M.H. Tsai, J.W. Yeh, High-entropy alloys: a critical review, *Mater. Res. Lett.* 2 (3) (2014) 107–123.
- [12] W.R. Wang, W.L. Wang, J.W. Yeh, Phases, microstructure and mechanical properties of  $\text{Al}_x\text{CoCrFeNi}$  high-entropy alloys at elevated temperatures, *J. Alloys Compd.* 589 (2014) 143–152.
- [13] W.R. Wang, W.L. Wang, S.C. Wang, et al., Effects of Al addition on the microstructure and mechanical property of  $\text{Al}_x\text{CoCrFeNi}$  high-entropy alloys, *Intermetallics* 26 (2012) 44–51.
- [14] X.Z. Zhang, D.T. Wang, H. Nagaumi, et al., Morphology, thermal stability, electronic structure and mechanical properties of alpha-AlFeMnSi phases with varying Mn/Fe atomic ratios: experimental studies and DFT calculations, *J. Alloys Compd.* 901 (2022) 11.
- [15] J.C. Li, Y.L. Li, F.F. Wang, et al., Friction stir processing of high-entropy alloy reinforced aluminum matrix composites for mechanical properties enhancement, *Mater. Sci. Eng.* 792 (2020) 8.
- [16] Y.Z. Liu, J. Chen, Z. Li, et al., Formation of transition layer and its effect on mechanical properties of  $\text{AlCoCrFeNi}$  high-entropy alloy/Al composites, *J. Alloys Compd.* 780 (2019) 558–564.
- [17] Z. Ma, Z.W. Yuan, X.K. Ma, et al., Interface characteristics and mechanical properties of  $\text{Al}_{0.6}\text{CoCrFeNi}/5052\text{Al}$  matrix composites fabricated via vacuum hot-pressing sintering and annealing, *Mater. Sci. Eng.* 859 (2022) 15.
- [18] M. Sau, E.D. Hintsala, Y.X. Chen, et al., High-Throughput nanoindentation mapping of additively manufactured T91 steel, *J. Occup. Med.* 74 (4) (2022) 1469–1476.
- [19] L. Chen, X.W. Zhang, Y.Y. Wang, et al., Microstructure and elastic constants of  $\text{AlTiVMoNb}$  refractory high-entropy alloy coating on Ti6Al4V by laser cladding, *Mater. Res. Express* 6 (11) (2019) 10.
- [20] X. Yang, H.X. Zhang, P. Dong, et al., A study on the formation of multiple intermetallic compounds of friction stir processed high entropy alloy particles reinforced Al matrix composites, *Mater. Char.* 183 (2022) 11.
- [21] H. Karimi Zarchi, M. Jalaly, M. Soltanieh, et al., Comparison of the activation energies of the formation of chromium carbide coating on carburized and uncarbured AISI 1020 steel, *Steel Res. Int.* 80 (11) (2009) 859–864.
- [22] A. Panteli, J.D. Robson, I. Brough, et al., The effect of high strain rate deformation on intermetallic reaction during ultrasonic welding aluminium to magnesium, *Mater. Sci. Eng.* 556 (2012) 31–42.
- [23] W. Chen, Z. Li, T. Lu, et al., Effect of ball milling on microstructure and mechanical properties of 6061Al matrix composites reinforced with high-entropy alloy particles, *Mater. Sci. Eng.* 762 (2019), 138116.
- [24] P. Han, W. Wang, Z. Liu, et al., Modification of cold-sprayed high-entropy alloy particles reinforced aluminum matrix composites via friction stir processing, *J. Alloys Compd.* 907 (2022), 164426.
- [25] Q. Li, T. Zhang, J. Qiao, et al., Mechanical properties and deformation behavior of dual-phase  $\text{Al}_{0.6}\text{CoCrFeNi}$  high-entropy alloys with heterogeneous structure at room and cryogenic temperatures, *J. Alloys Compd.* 816 (2020), 152663.
- [26] J. Ruzic, S. Emura, X. Ji, et al., Mo segregation and distribution in Ti-Mo alloy investigated using nanoindentation, *Mater. Sci. Eng.* 718 (2018) 48–55.
- [27] A. Davoodi, Z. Esfahani, M. Sarvghad, Microstructure and corrosion characterization of the interfacial region in dissimilar friction stir welded AA5083 to AA7023, *Corrosion Sci.* 107 (2016) 133–144.
- [28] R. Fernandez, S. Cabeza, T. Mishurova, et al., Residual stress and yield strength evolution with annealing treatments in an age-hardenable aluminum alloy matrix composite, *Mater. Sci. Eng.* 731 (2018) 344–350.
- [29] F. Zhang, B.Y. Zhang, X.P. Chen, et al., Computational simulation of voids formation and evolution in Kirkendall effect, *Phys. Stat. Mech. Appl.* 554 (2020) 11.
- [30] C. a. C. Sequeira, L. Amaral, Role of Kirkendall effect in diffusion processes in solids, *Trans. Nonferrous Metals Soc. China* 24 (1) (2014) 1–11.
- [31] C. Frick, B. Clark, S. Orso, et al., Size effect on strength and strain hardening of small-scale [1 1 1] nickel compression pillars, *Mater. Sci. Eng.* 489 (1–2) (2008) 319–329.
- [32] A.M. Giwa, P.K. Liaw, K.A. Dahmen, et al., Microstructure and small-scale size effects in plasticity of individual phases of  $\text{Al}_{0.7}\text{CoCrFeNi}$  high entropy alloy, *Extreme Mech. Lett.* 8 (2016) 220–228.
- [33] C. Yan, B. Bor, A. Plunkett, et al., Nanoindentation of supercrystalline nanocomposites: linear relationship between elastic modulus and hardness, *J. Occup. Med. 74* (6) (2022) 2261–2276.
- [34] J.J. Roa, P.S. Phani, W.C. Oliver, et al., Mapping of mechanical properties at microstructural length scale in WC-Co cemented carbides: assessment of hardness and elastic modulus by means of high speed massive nanoindentation and statistical analysis, *Int. J. Refract. Metals Hard Mater.* 75 (2018) 211–217.
- [35] A. Orozco-Caballero, C. Gutierrez, B. Gan, et al., High-throughput nanoindentation mapping of cast IN718 nickel-based superalloys: influence of the Nb concentration, *J. Mater. Res.* 36 (11) (2021) 2213–2222.
- [36] W.C. Oliver, G.M. Pharr, An improved technique for determining hardness and elastic modulus using load and displacement sensing indentation experiments, *J. Mater. Res.* 7 (6) (1992) 1564–1583.
- [37] X.Q. Chen, H.Y. Niu, D.Z. Li, et al., Modeling hardness of polycrystalline materials and bulk metallic glasses, *Intermetallics* 19 (9) (2011) 1275–1281.
- [38] Y. Rong, Z. Taihua, J. Peng, et al., Experimental verification and theoretical analysis of the relationships between hardness, elastic modulus, and the work of indentation, *Appl. Phys. Lett.* 92 (23) (2008), 231906.
- [39] D. Labonte, A.K. Lenz, M.L. Oyen, On the relationship between indentation hardness and modulus, and the damage resistance of biological materials, *Acta Biomater.* 57 (2017) 373–383.
- [40] P.Y. Cao, X.D. Ni, F.Y. Tian, et al., Ab initio study of  $\text{Al}_x\text{MoNbTiV}$  high-entropy alloys, *J. Phys.-Condensed Matter* 27 (7) (2015) 6.
- [41] F. Tian, L. Delcug, N. Chen, et al., Structural stability of  $\text{NiCoFeCrAl}_x$  high-entropy alloy from ab initio theory, *Phys. Rev. B* 88 (8) (2013), 085128.
- [42] B. Baran, T. Ertürk, Y. Sarikaya, et al., Workability test method for metals applied to examine a workability measure (plastic limit) for clays, *Appl. Clay Sci.* 20 (1–2) (2001) 53–63.
- [43] Q.Y. Li, J. Li, G. He, Compressive properties and damping capacities of magnesium reinforced with continuous steel wire, *Mater. Sci. Eng.* 680 (2017) 92–96.

- [44] M. Tiegel, R. Hosseiniabadi, S. Kuhn, et al., Young's modulus, Vickers hardness and indentation fracture toughness of alumino silicate glasses, *Ceram. Int.* 41 (6) (2015) 7267–7275.
- [45] S. Karan, S.P. Sen Gupta, Vickers microhardness studies on solution-grown single crystals of magnesium sulphate hepta-hydrate, *Mater. Sci. Eng.* 398 (1–2) (2005) 198–203.
- [46] G. Ben Ghorbal, A. Tricoteaux, A. Thuault, et al., Comparison of conventional Knoop and Vickers hardness of ceramic materials, *J. Eur. Ceram. Soc.* 37 (6) (2017) 2531–2535.
- [47] J.M. Schneider, M. Bigerelle, A. Iost, Statistical analysis of the Vickers hardness, *Mater. Sci. Eng.* A262 (1–2) (1999) 256–263.
- [48] Y. Li, Y.H. Zhao, V. Ortalan, et al., Investigation of aluminum-based nanocomposites with ultra-high strength, *Mater. Sci. Eng.* 527 (1–2) (2009) 305–316.
- [49] T. Thankachana, K. Sooryaprakash, C. Saranya, et al., Mathematical analysis on the effect of tin on mechanical, electrical and thermal properties in magnesium-tin alloys, *Materials Discovery* 12 (2018) 55–62.
- [50] Z.W. Yuan, H. Liu, Z. Ma, et al., Microstructure and properties of high entropy alloy reinforced titanium matrix composites, *Mater. Char.* 187 (2022) 10.
- [51] Z.C. Li, S.N. White, Mechanical properties of dental luting cements, *J. Prosthet. Dent* 81 (5) (1999) 597–609.